

Integral field spectroscopy of local LCBGs: NGC 7673, a case study. Physical properties of star-forming regions

A. Castillo-Morales,^{1*} J. Gallego,¹ J. Pérez-Gallego,² R. Guzmán,²
J. C. Muñoz-Mateos,^{1,3} J. Zamorano¹ and S. F. Sánchez⁴

¹*Dpto. de Astrofísica y CC. de la Atmósfera, Universidad Complutense de Madrid, Spain*

²*University of Florida, 211 Bryant Space Science Center, FL 32611-2055, Gainesville, USA*

³*National Radio Astronomy Observatory, 520 Edgemont Road, Charlottesville, VA 22903-2475, USA*

⁴*Centro Astronómico Hispano Alemán, AIE (CSIC-MPG), E-04004 Almería, Spain*

Accepted 2010 October 1. Received 2010 September 27; in original form 2010 January 10

ABSTRACT

Physical properties of the star-forming regions in the local Luminous Compact Blue Galaxy (LCBG) NGC 7673 are studied in detail using 3D spectroscopic data taken with the PMAS fibre pack (PPAK) integral field unit at the 3.5-m telescope in the Centro Astronómico Hispano Alemán (CAHA). We derive integrated and spatially resolved properties such as extinction, star formation rate (SFR) and metallicity for this galaxy. Our data show an extinction map with maximum values located at the position of the main clumps of star formation showing small spatial variations [$E(B - V)_t = 0.12\text{--}0.21$ mag]. We derive an $H\alpha$ -based SFR for this galaxy of $6.2 \pm 0.8 M_\odot \text{ yr}^{-1}$ in agreement with the SFR derived from infrared and radio continuum fluxes. The star formation is located mainly in clumps A, B, C and F. Different properties measured in clump B make this region peculiar. We find the highest $H\alpha$ luminosity with an SFR surface density of $0.5 M_\odot \text{ yr}^{-1} \text{ kpc}^{-2}$ in this clump. In our previous work, the kinematic analysis for this galaxy shows an asymmetrical ionized gas velocity field with a kinematic decoupled component located at the position of clump B. This region shows the absence of strong absorption features and the presence of a Wolf–Rayet stellar population indicating that this is a young burst of massive stars. Furthermore, we estimate a gas metallicity of $12 + \log(\text{O}/\text{H}) = 8.20 \pm 0.15$ (0.32 solar) for the integrated galaxy using the R23 index. The values derived for the different clumps with this method show small metallicity variations in this galaxy, with values in the range 8.12 (for clump A) to 8.23 (for clump B) for $12 + \log(\text{O}/\text{H})$. The analysis of the emission-line ratios discards the presence of any active galactic nuclei (AGN) activity or shocks as the ionization source in this galaxy. Between the possible mechanisms to explain the starburst activity in this galaxy, our 3D spectroscopic data support the scenario of an on-going interaction with the possibility for clump B to be the dwarf satellite galaxy.

Key words: galaxies: individual: NGC 7673 – galaxies: starburst.

1 INTRODUCTION

Starburst galaxies are those in which star formation and associated phenomena dominate the total energetics (Weedman 1983). These galaxies have larger star formation rates (SFRs) per unit area than normal galaxies, and to produce their current stellar masses at their current SFRs they would take much less than the age of the Universe (Kennicutt 1998b). Starburst galaxies are found at different redshifts, which denotes their cosmological relevance, and turn those found nearby into perfect candidates to study the mysteries of

the star formation process throughout time when they can be equally and properly selected at different epochs of the Universe. Both distant Lyman Break Galaxies (LBGs; Steidel et al. 1996; Lowenthal et al. 1997) and closer Luminous Compact Blue Galaxies (LCBGs; Werk, Jangren & Salzer 2004) fall into this category.

LCBGs are, as described by Werk et al. (2004), galaxies with (i) absolute blue magnitude (M_B) brighter than -18.5 , (ii) effective surface brightness (SB_e) brighter than $21 B\text{-mag arcsec}^{-2}$ and (iii) $(B - V)$ colour bluer than 0.6. In an observational parameter space defined by these observational properties [i.e. M_B , SB_e and $(B - V)$] LCBGs and distant LBGs share the same optical properties. Galaxies belonging to this population (i) are morphologically heterogeneous, (ii) form stars at around $10\text{--}20 M_\odot \text{ yr}^{-1}$, (iii) show

*E-mail: acm@astrax.fis.ucm.es

velocity widths of $30\text{--}120\text{ km s}^{-1}$, (iv) are as compact as $2\text{--}5\text{ kpc}$ and (v) have metallicities lower than solar.

LCBGs play an important role in galaxy evolution over cosmological time-scales, as has been shown by various observational studies in the last decade (Werk et al. 2004; Melbourne et al. 2007; Guzmán et al. 1997; Steidel et al. 2003). The lack of LCBGs in the local universe when compared to higher redshifts raises the issue of how this population has evolved in the last $9\text{--}10\text{ Gyr}$. There are two main suggested scenarios (not mutually exclusive): (i) LCBGs are the progenitors of today's spheroidal galaxies, low-mass ($M < 10^{10} M_{\odot}$) spheroidal galaxies or dwarf elliptical galaxies whose properties according to evolutionary models would be matched by a typical LCBG after a $4\text{--}6\text{ Gyr}$ fading process showing low metallicities (Koo et al. 1994; Guzmán et al. 1998; Noeske et al. 2006); and (ii) LCBGs are the progenitors of the spheroidal component of today's disc galaxies, present-day small spirals, more massive ($M \sim 10^{10} M_{\odot}$) than inferred from virial masses, whose emission is mostly due to a vigorous central burst (Phillips et al. 1997; Hammer et al. 2001; Puech et al. 2006). This scenario predicts higher metallicities than those likely to be observed in local dwarf galaxies (Kobulnicky & Zaritsky 1999).

Key ingredients on the discussion on whether LCBGs evolve one way or another are their mass and metallicity. A reliable determination of their masses and metallicities is necessary to properly place LCBGs within one evolution scenario or the other, or to understand what makes them evolve one way or another. Masses of LCBGs can be derived from their rotation curves and velocity widths; nevertheless one needs to be careful with those, since most of these objects' kinematics might not be coupled to their masses due to supernova galactic winds, and both minor and major mergers. The metallicity can be estimated in LCBGs by measuring the auroral emission-line flux $[\text{O III}]\lambda 4363$, which gives, along with the $[\text{O III}]\lambda\lambda 4959, 5007$ fluxes, a direct determination of the electron temperature. But beyond certain metallicities $[\text{O III}]\lambda 4363$ detection is not possible and the oxygen abundance must be empirically determined using strong emission lines through the use, for example, of the R23 indicator.

The knowledge not only of the integrated properties such as mass, metallicity, extinction or SFR, but also of their spatial distribution in the galaxy plays an important role in studying the nature of LCBGs. Integral field spectroscopy technique offers a great advantage in carrying out this issue. In this way, we are able to derive full maps of physical properties such as extinction to locate the dusty regions in these galaxies. This is important to properly compute the extinction-corrected emission-line maps and derive SFR and metallicity spatial distributions. 3D spectroscopy makes it possible to carry out this work in an efficient way allowing us to test model predictions on the origin and evolution of these massive starbursts.

Interest in LCBGs has multiplied following the initial observational results and the properties highlighted above, but their relation to today's galaxy population still remains unknown. In order to understand the nature of LCBGs and its role in galaxy evolution we have selected a representative sample of 22 LCBGs within 200 Mpc from the Sloan Digital Sky Survey (SDSS; Adelman-McCarthy, Agüeros & Allam 2006), Universidad Complutense de Madrid (UCM; Zamorano et al. 1994) and Markarian catalogues (Markarian et al. 1989) that best resemble the properties of distant LCBGs, ensuring that this sample, although small, is representative of the LCBG population as a class by covering the whole range in luminosity, colour, surface brightness and environment [see Pérez-Gallego et al. (2010, hereafter PG10) for more details on the sample selection]. We are carrying out a multi-wavelength study of

Table 1. NGC 7673 observational properties. Redshift (z) from Huchra, Vogeley & Geller (1999). Absolute B magnitude $M(B)$, effective surface brightness SB_e , colour index $(B - V)$ and effective radius R_e from Pisano et al. (2001).

Name	NGC 7673
z	0.011368
$M(B)$	-20.50 mag
SB_e	$19.40\text{ mag arcsec}^{-2}$
$(B - V)$	0.30 mag
R_e	1.9 kpc

this sample including not only the optical, but also the millimetre and centimetre ranges (e.g. Garland et al. 2007). Arguably, one of the most important aspects of this study and the one we focus on this paper is the optical 3D spectroscopy. The optical is the best understood spectral range in nearby galaxies, and will be systematically studied at high z with the new generation of near-infrared multi-object spectrographs and integral field units in 10-m class telescopes (Förster Schreiber et al. 2006; Puech et al. 2006).

In this paper, we focus on the physical properties of the star-forming regions of LCBG NGC 7673. We use integral field spectroscopy data which allow us to study both the integrated and the spatially resolved properties, such as extinction, SFR and gas metallicity. The detailed analysis of these properties together with the kinematic analysis of the ionized gas discussed in PG10 will help to understand the starburst nature of this galaxy.

NGC 7673, also known as UCM2325+2318 and Mrk 325, is a nearby ($z = 0.011368$) starburst galaxy widely studied in the past (e.g. Duflot-Augarde & Alloin 1982; Homeier & Gallagher 1999; Homeier, Gallagher & Pasquali 2002; Pasquali & Castangia 2008). The small size, high surface brightness, strong emission lines and blue colours make NGC 7673 a prototypical LCBG (see Table 1).

The starburst activity in this galaxy is located within a circle of 3.7 kpc radius ($\approx 2 \times R_e$, where R_e is the effective radius). It shows a clumpy structure with star-forming regions visible in optical as bright knots in the galactic disc (Pérez-González et al. 2003, detected 87 distinct star-forming knots in a deep $H\alpha$ image of this galaxy). Homeier et al. (2002) identified 50 star cluster candidates working on *Hubble Space Telescope* (HST)/WFPC2 images, where the bluer and brighter clusters are strongly concentrated into the main starburst 'clumps' (see Fig. 1). From previous ground-based images (Duflot-Augarde & Alloin 1982), six main clumps have been identified, A,B,C,D,E,F (see their fig. 1), and will be referred to in this paper.

The cosmology used in this paper is $H_0 = 70\text{ km s}^{-1}\text{ Mpc}^{-1}$. The recession velocity of 3408 km s^{-1} from NASA/IPAC Extragalactic Data base implies a distance of $d = 49\text{ Mpc}$, and a projected scale of 250 pc per arcsec for this galaxy. This paper is structured as follows. Observations and data reduction are described in Section 2. Our measurements are shown in Section 3. The results and discussion are given in Sections 4 and 5. Finally, Section 6 shows the summary of our work.

2 OBSERVATIONS AND DATA REDUCTION

Objects from our sample were observed using PPAK (Kelz et al. 2006), a fibre-based system for integral field spectroscopy

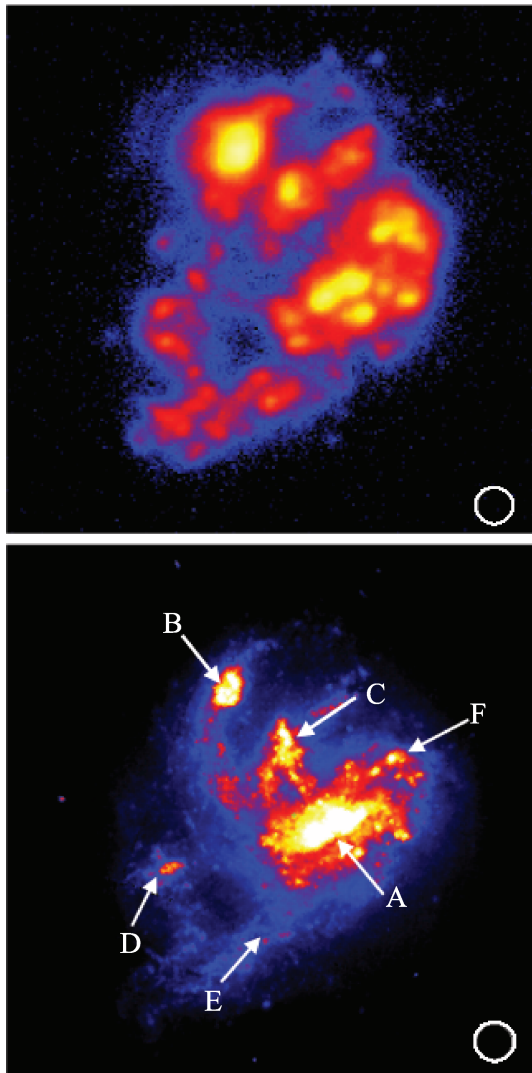


Figure 1. Top: $H\alpha$ image from the NOT Telescope (Pérez-González et al. 2003). Bottom: optical image (*WPC2*, *F555W* filter) from *HST*. The positions of the main clumps A to F are indicated. Both images are 40×40 arcsec² and the PPAK fibre (2.7 arcsec diameter) is plotted at the right bottom corner.

operating at the 3.5-m CAHA telescope.¹ The field of view of PPAK, as well as its good spatial and spectral resolution, is optimum for the observation of our sample galaxies with typical half-light diameters of around 10 to 30 arcsec, and velocity widths ranging from 60 to 120 km s⁻¹. PPAK consists of 331 scientific fibres each of 2.7 arcsec in diameter, covering a hexagonal area of 74×65 arcsec on the sky. In addition, there are 15 calibration fibres and 36 fibres grouped in six bundles located at ≈ 90 arcsec of the centre of the science bundle that are used to measure the sky simultaneously.

PPAK observations of NGC 7673 were made over the nights of 2005 August 10 and 11 using two different setups. First, a 300 lines mm⁻¹ grating (V300) centred at 5316 Å was used. This low-

resolution configuration provided a spectral resolution of 10.7 Å full width at half-maximum (FWHM) covering from 3600 to 7000 Å and allowed us to measure all the emission-line ratios in one single spectrum, avoiding uncertainties associated with flux calibration and spectral response between different spectral ranges obtained with different configurations. Secondly, a 1200 lines mm⁻¹ grating (V1200) centred at 5040 Å was used. This intermediate-resolution configuration provided a nominal spectral resolution of 2.78 Å FWHM (i.e. $\sigma \sim 75$ km s⁻¹ at $H\beta$), covering from 4900 to 5400 Å. Three different dithering positions were observed in both spectral configurations (see table 2 in PG10 for more observational details.)

The data reduction of 2D fibre spectra was done using the IRAF² environment, R3D and EURO3D software (Sánchez 2004) following the techniques described in Sánchez (2006). The standard procedure consists of the following steps: bias subtraction, spectra extraction, wavelength calibration (see PG10 for more data reduction details in this step), fibre-to-fibre correction and sky emission subtraction.

The aforementioned data reduction steps are done for each individual dithering exposure. The following steps instead are done using the information of the three dithering exposures to compute a final data cube absolute flux calibrated.

(i) *Flux calibration.* PPAK is based on pure fibre bundles and does not cover the entire field of view, which imposes flux losses. Nevertheless, our observational technique of dithering allows us to cover the complete field of view in three exposures. Therefore, our first approach is to determine a relative spectrophotometric calibration for each dithering exposure and recalibrate the spectra later, using additional information coming from broad-band photometry. The relative flux calibration requires the observation of a standard spectrophotometric calibration star. We apply all the previous reduction steps to the calibration star frame. We compare the measured spectrum of the star (flux coming from several fibres) with the absolute values and determine the ratio between counts per second and flux. In this way we get the instrumental response which is applied to science frames to flux calibrate them. To perform an absolute flux calibration we compute broad-band PPAK maps in *B*, *V* and *R* filters. For *B* and *R* broad-band maps, fluxes obtained in different circular apertures over the PPAK field of view are compared with fluxes computed over the Jacobus Kapteyn Telescope (JKT) (*B* band) and the Nordic Optical Telescope (NOT) (*R* band) at La Palma, from Pérez-González et al. (2000, 2003) with the same apertures. JKT and NOT images were registered taking as a reference the PPAK map and then convolved with a Gaussian filter to match the spatial resolution of PPAK. For *V*-band filter the Huchra (1977) tabulated value, $m_V = 13.11$, is compared with the apparent magnitude computed from the PPAK *V*-band map. The comparison of relative PPAK fluxes with absolute fluxes in different photometric bands and in different apertures gives a mean factor of 0.44 with a standard deviation of 0.04, i.e. PPAK fluxes need to be multiplied by this factor to match absolute fluxes. We compared the absolute PPAK $H\alpha$ emission fluxes computed in different apertures with the fluxes from the $H\alpha$ narrow-band image from Pérez-González et al. (2003). In this case PPAK fluxes are ≈ 15 per cent smaller compared with those in the $H\alpha$ narrow-band image.

(ii) *Locating the spectra in the sky.* The location of the spectra in the sky is given by a position table that relates each spectrum with a certain fibre. Since we use the observational technique of dithering

¹ Based on observations collected at the German–Spanish Astronomical Center, Calar Alto, jointly operated by the Max-Planck-Institut für Astronomie Heidelberg and the Instituto de Astrofísica de Andalucía (IAA/CSIC).

² IRAF is distributed by the National Optical Astronomy Observatories.

exposures in order to cover the complete field of view, the next step in the data reduction is to create a data cube with the information for the three ditherings. This is done through the *regularization* of the data: a grid of $1 \text{ arcsec pixel}^{-1}$ is constructed over the field of view of the dithered exposures. Then, for each pixel of this grid, the spectra that cover the pixel are averaged (weighted by the fraction of pixel area in each dithering), obtaining a final data cube. This *regularization* does not imply any interpolation. Finally, we obtain a data cube with a spectrum in each pixel where the exposure time for each pixel is different, depending on whether it has been covered by one, two or three fibres.

(iii) *Differential Atmospheric Refraction (DAR) correction*. This correction is done by tracing the location of the intensity peak of a reference object in the field of view along the spectral range. These locations are estimated by determining the centroid of the object in the image slice extracted at each wavelength from the data cube. Then, the full data cube is shifted to a common reference by re-sampling and shifting each image slice at each wavelength using an interpolation scheme in the spatial direction. In the case of V300 configuration we apply maximum shifts of 0.2 and 0.4 arcsec in the x - and y -axis, respectively. For V1200 configuration we checked DAR correction is not required with shifts smaller than 0.1 arcsec.

3 DATA MEASUREMENTS

For each spectrum, different quantities such as emission-line flux, continuum flux and equivalent width were measured by fitting single Gaussian functions to the observed emission-line profiles using our own software. A two-component (emission and absorption) Gaussian fit was performed in order to correct the Balmer lines emission for underlying stellar absorption (see Section 3.1).

Here, we analyze in detail the high-resolution images obtained with the *Hubble Space Telescope* (*HST*) in the optical (WFPC2, F555W) and the NOT Telescope in $H\alpha$ (see Fig. 1) in order to match the spatial position of each clump with the starburst identified in the $H\alpha$ image. Clump A is composed by several distinct $H\alpha$ knots, with three of them located in the central structure of the bar shape region. In the optical high-resolution *HST* image, two bright regions can be distinguished in this area. Clump B shows a strong $H\alpha$ emission located in one bright knot. The *HST* image shows clump B to be clumpy with a central peak of emission surrounded by two bright shells. It seems to be situated in a spiral arm connecting this region with the central structure. Clump C is another strong $H\alpha$ emission region which shows several knots in the optical *HST* image. In Clump D the $H\alpha$ emission is not seen at the centre of the clump but at the edges. Clump E defined in Duflot-Augarde & Alloin (1982) can be seen in the optical image as a region of faint emission connected to the central structure. Nevertheless, this area is not associated with any $H\alpha$ emission region in particular. At this location (SE of the galaxy) there are several knots of $H\alpha$ emission. Finally clump F is an extended star formation region composed of many clusters and dominated by a single object (Homeier et al. 2002) embedded in a strong $H\alpha$ emitting region.

The spatial location of each clump in this paper is selected using the B -band and $H\alpha$ PPAK maps (see Fig. 2). The spectrum corresponding to each clump is computed by adding up the spectrum from several pixels (see Fig. 3). The integrated spectrum of the galaxy is computed co-adding the spectra of all pixels in PPAK data set over the full field of view.

The properties computed for different clumps in the following sections are derived from the analysis of the spectrum corresponding to each clump. Moreover, we have checked the agreement with the

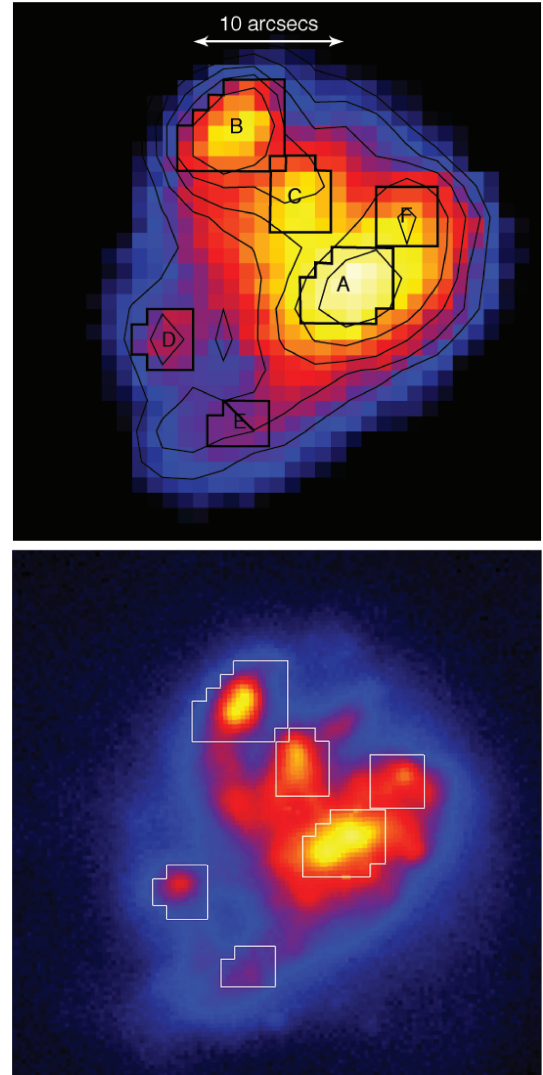


Figure 2. Top: PPAK B -band continuum map and $H\alpha$ emission overlaid in contours. The positions of the main clumps A to F are indicated. Bottom: JKT B -band image from Pérez-González et al. (2000). North is up and east is left.

same properties derived from the mean values obtained from the computed map in the regions where the clumps are located.

3.1 Stellar absorption correction

To obtain an accurate value of the fluxes of the Balmer emission lines we take into account the presence of an underlying stellar absorption. The stellar absorption can considerably affect the calculation of quantities such as the extinction. To solve this problem, two Gaussian functions are fitted in those cases where the absorption wings are visible (for example, that is the case for the $H\beta$ Balmer line). For this purpose we use the V1200 configuration data cube whose spectral resolution ($\text{FWHM} \approx 2.5 \text{ \AA}$) allows us to better fit the absorption wings in the $H\beta$ Balmer line.

For each spectrum with enough signal-to-noise ratio (S/N larger than 15 in the continuum), two different fits are performed. First, the $H\beta$ Balmer line is fitted only with a Gaussian model in emission. Secondly, the same data are fitted with two Gaussian models, one in emission and another in absorption. We tied the centroids of the

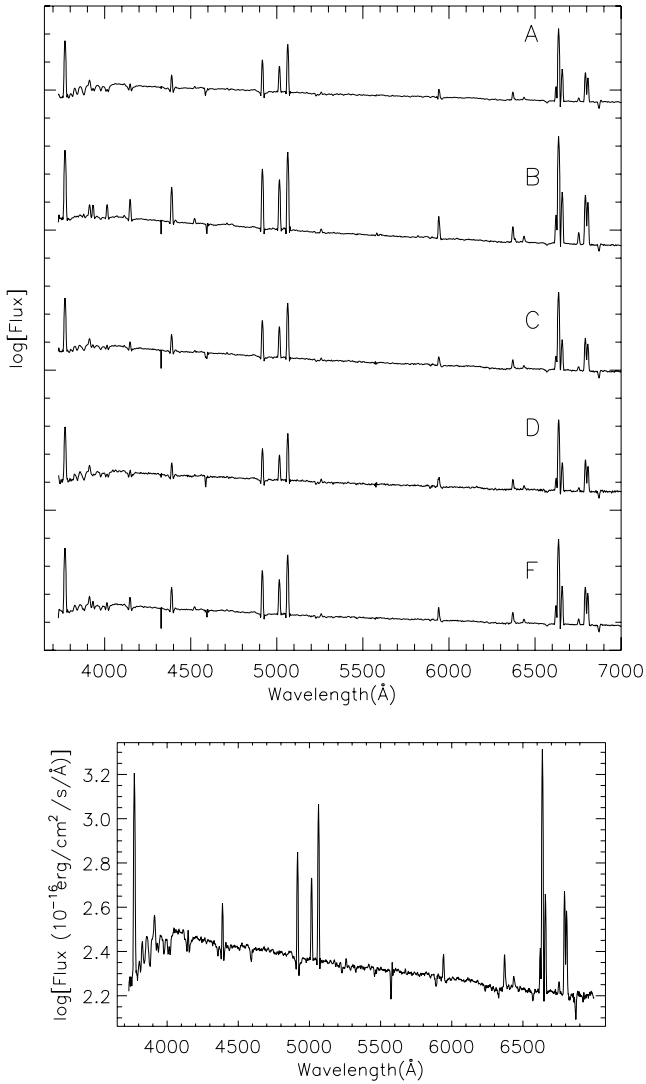


Figure 3. Upper panel: spectra (in logarithmic scale and arbitrarily scaled for better visualization) of different clumps in NGC 7673 obtained summing up the spectra from some pixels defining these regions. Bottom panel: integrated spectrum (in logarithmic scale) of NGC 7673 obtained co-adding all individual spectra of PPAK data set over the full field of view. All the spectra shown here are obtained with the V300 grating configuration providing a nominal spectral resolution of 10.7 Å FWHM .

Gaussian in emission and absorption to be the same. The Gaussian absorption width is upper limited to the value found when the total galaxy spectrum is fitted and pixels located at the wings of the $H\beta$ absorption are double weighted. The best fit is based in a χ^2 scheme, and we accept the two Gaussian fit as the best fit when the reduced χ^2 improves at least by 15 per cent with respect to the single Gaussian fit. All the spectra in our data cube are fitted with two Gaussian except the spectra corresponding to clump B, where we fit only a single Gaussian in emission and then the $H\beta$ absorption equivalent width is considered to be zero or negligible.

The goodness of our fitting method is checked using simulated spectra. With S/N larger than 15 in the continuum, this method is able to measure absorption equivalent widths as small as $\approx 2.5 \text{ Å}$ with relative uncertainties smaller than 15 per cent. For larger absorption equivalent widths the uncertainty decreases: for $EW_{\text{abs}} > 4 \text{ Å}$ we find a less than 10 per cent relative error.

In Fig. 4, the $H\beta$ absorption equivalent width (EW_{abs}) map and some representative fits in different regions are shown. The EW_{abs} values are in the range $0\text{--}6.6 \text{ Å}$.

Dufloot-Augarde & Alloin (1982) employed a crude method to find $EW_{\text{abs}} \approx 8 \text{ Å}$ for the $H\beta$ Balmer line in clump A and find no evidence of absorption wings in clumps B, C and D. In Table 2, we summarize the $H\beta$ absorption equivalent widths found for different clumps and the integrated galaxy spectrum. These values are measured fitting the spectra corresponding to each clump. While in clump B the underlying Balmer absorption is clearly less important, in other regions the stellar absorption is more significant, with computed values of $EW_{\text{abs}} \approx 5.6 \text{ Å}$ in clump A, or 6.5 Å in regions between clumps A and D. When the integrated galaxy spectrum is fitted the $H\beta$ absorption equivalent width is $4.8 \pm 0.5 \text{ Å}$.

3.2 Emission-line fluxes

In this paper, we focus on the study of the physical properties of the gas through the analysis of the observed emission lines. In the V300 setup configuration the main emission lines observed are: $[O \text{ II}]\lambda 3727$, $H\beta$, $[O \text{ III}]\lambda\lambda 4959, 5007$, $[He \text{ I}]\lambda 5876$, $[O \text{ I}]\lambda 6300$, $H\alpha$, $[N \text{ II}]\lambda\lambda 6548, 6584$, $[S \text{ II}]\lambda\lambda 6717, 6731$. The wide wavelength range of this configuration allows us to derive not only line emission fluxes maps but also line emission ratios in a consistent way.

The emission lines in each spectrum of the data cube were fitted by single Gaussian profiles using our own software tools. We calculate the error in the line fluxes from the quadratic sum of the error coming from the absolute flux calibration and the error from the expression $\sigma_l = \sigma_c N^{1/2} [1 + EW/N\Delta]^{1/2}$ (Castellanos 2000) where σ_c is the standard deviation in a box centred close to the measured emission line; N is the number of pixels used in the measurement of the line flux; EW is the equivalent width of the line and Δ is the wavelength dispersion in Å pixel^{-1} . Only the spectra with a minimum S/N of 15 in the flux detection are considered to ensure a relative uncertainty less than 10 per cent in the flux determination.

Some of the emission lines are fitted simultaneously ($H\alpha + [N \text{ II}]\lambda\lambda 6548, 6584$, $[O \text{ III}]\lambda\lambda 4959, 5007$, $[S \text{ II}]\lambda\lambda 6717, 6731$). In this case, the best fit is found by forcing all the lines fitted simultaneously to have the same velocity shift and width. The continuum under the emission line was fitted at the same time using a linear or quadratic function.

We perform a pixel-to-pixel correction to the $H\beta$ and $H\alpha$ emission-line fluxes computed from the V300 data cube using the stellar absorption EW computed from $H\beta$ Balmer line Gaussian fits in the V1200 data cube as explained in Section 3.1. We assume the stellar absorption correction in $H\beta$ and $H\alpha$ is the same [Kurucz (1992) established that the $H\alpha$ and $H\beta$ equivalent widths are equal within a 30 per cent uncertainty]. In the case of $H\alpha$ emission, the stellar absorption corrected fluxes are not significantly different from the uncorrected fluxes (relative differences are in the range $0\text{--}15$ per cent with 5 per cent relative difference for the integrated galaxy flux). For $H\beta$ emission fluxes the differences are much larger with relative differences over 30 per cent for the integrated galaxy flux and the majority of pixels except for clump B (0 per cent) and clump F (15 per cent). To estimate the error in the $H\alpha$ and $H\beta$ absorption-corrected fluxes we take into account the uncertainties from the absorption equivalent width and continuum flux. The main source of error is coming from the uncertainty in the absolute flux calibration.

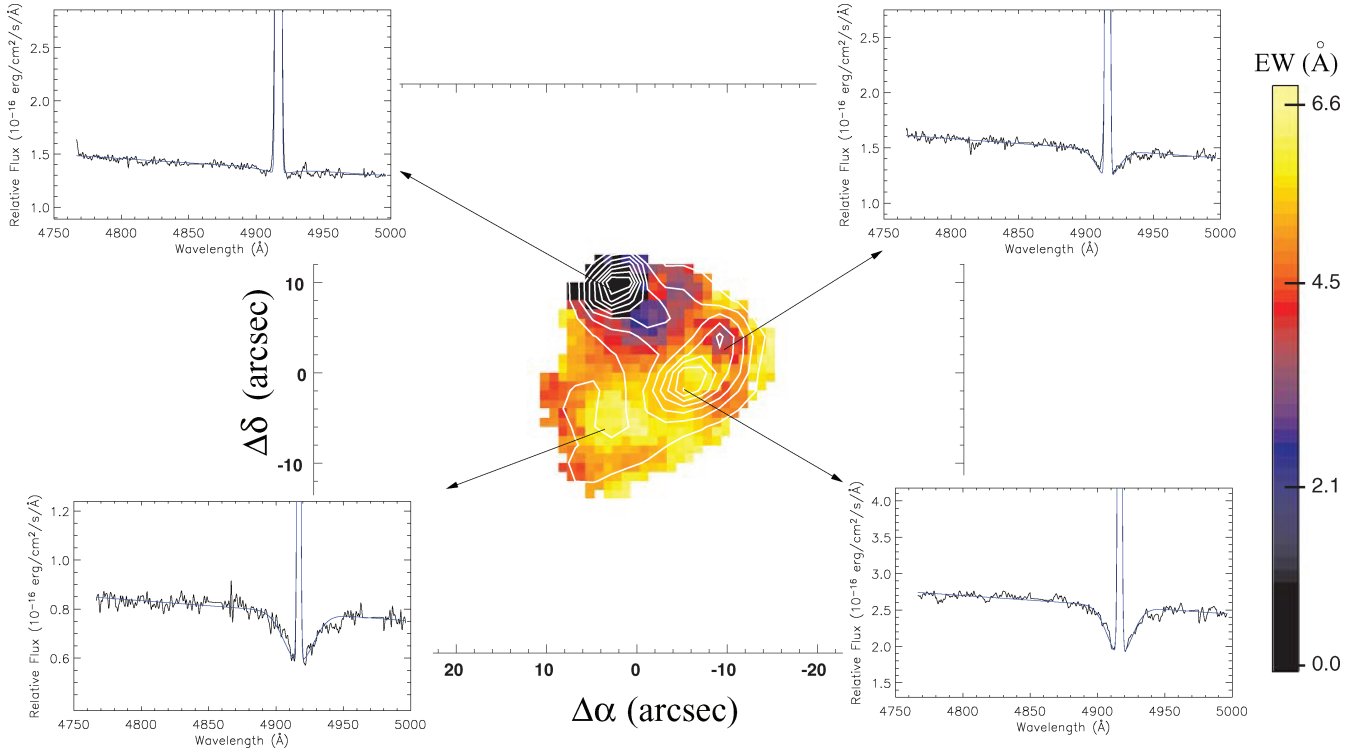


Figure 4. $H\beta$ stellar absorption equivalent width map computed from the double Gaussian fit method described in Section 3.1. Contours from $H\alpha$ emission are overplotted in white colour. Fitted spectra from different regions in NGC 7673 are shown.

Table 2. Summary of PPAK results for NGC 7673 and the main clumps. Col. 1: region from which the spectrum is analysed. Col. 2: measured stellar absorption equivalent width for $H\beta$ Balmer line in Å. Col. 3: measured emission equivalent width for $H\alpha$ Balmer line with typical errors of 0.5 Å. Col. 4: colour excess obtained from the $F(H\alpha)/F(H\beta)$ ratio. Col. 5: extinction-corrected $H\beta$ luminosity in units of $10^{41} \text{ erg s}^{-1}$. Col. 6: extinction-corrected $H\alpha$ luminosity in units of $10^{41} \text{ erg s}^{-1}$. Col. 7: SFR in $M_{\odot} \text{ yr}^{-1}$ computed from extinction-corrected $H\alpha$ flux. Col. 8: SFR surface density in $M_{\odot} \text{ yr}^{-1} \text{ kpc}^{-2}$. Cols 9, 10 and 11: emission-line ratios computed from the extinction-corrected fluxes.

Region (1)	EW_{abs} (2)	$EW(H\alpha)$ (3)	$E(B - V)$ (4)	$L(H\beta)$ (5)	$L(H\alpha)$ (6)	SFR (7)	Σ_{SFR} (8)	$\frac{[N\text{II}]\lambda 6584}{H\alpha}$ (9)	$\frac{[O\text{III}]\lambda 5007}{H\beta}$ (10)	$\frac{[S\text{II}]\lambda\lambda 6716, 6731}{H\alpha}$ (11)
NGC 7673	4.8 ± 0.5	106	0.17 ± 0.03	2.7 ± 0.4	7.8 ± 0.9	6.2 ± 0.8	0.08	0.15	1.6	0.27
Clump A	5.6 ± 0.6	104	0.19 ± 0.03	0.36 ± 0.05	1.0 ± 0.1	0.8 ± 0.1	0.49	0.17	1.6	0.24
Clump B	0.0	427	0.21 ± 0.01	0.52 ± 0.06	1.5 ± 0.1	1.2 ± 0.1	0.52	0.12	1.9	0.18
Clump C	3.1 ± 0.5	111	0.16 ± 0.03	0.11 ± 0.02	0.33 ± 0.04	0.26 ± 0.03	0.23	0.13	1.7	0.24
Clump D	5.1 ± 0.5	111	0.12 ± 0.03	0.034 ± 0.005	0.10 ± 0.01	0.08 ± 0.01	0.09	0.14	1.7	0.27
Clump E	5.2 ± 0.5	113	0.20 ± 0.03	0.032 ± 0.005	0.09 ± 0.01	0.07 ± 0.01	0.10	0.17	1.2	0.31
Clump F	4.1 ± 0.4	171	0.20 ± 0.02	0.17 ± 0.02	0.48 ± 0.05	0.38 ± 0.04	0.38	0.14	1.7	0.24

3.3 Maps generation

Finally, we generate maps of spectral features such as emission-line fluxes, stellar absorption equivalent widths, extinction and other properties from the *regularized* flux-calibrated data cube using our own software tools. Once we have a collection of values with the information of the measured spectral feature in each pixel we can represent them using the relative position of each pixel in the sky. The computed maps consist of a 72×63 pixels grid where the spatial resolution element (fibre size of 2.7 arcsec) is sampled by approximately 3×3 pixels. We decide to work with the spectral information in each pixel instead of in each fibre due to the application of DAR correction as it is explained in Section 2.

To be able to compare our generated PPAK maps with other images we perform an astrometric calibration of our PPAK images using the $H\alpha$ emission PPAK map and the $H\alpha$ narrow-band image

from NOT (Pérez-González et al. 2003) with known astrometry. The NOT image is convolved with a Gaussian kernel function to match the PPAK spatial resolution. The positions of different $H\text{II}$ regions in both images PPAK and NOT are used to compute an astrometric solution using several tasks in IRAF package. The astrometric calibration is done by forcing the same x and y scale ($1 \text{ arcsec pixel}^{-1}$) with an error given by an *rms* of 0.09 and 0.14 arcsec in the x and y axes, respectively.

4 RESULTS

4.1 Extinction map

From the purpose of correcting for dust extinction the observed emission lines, we have derived the total colour excess $[E(B - V)]_{\text{t}}$, i.e. the sum of the intrinsic and foreground Galactic reddening from

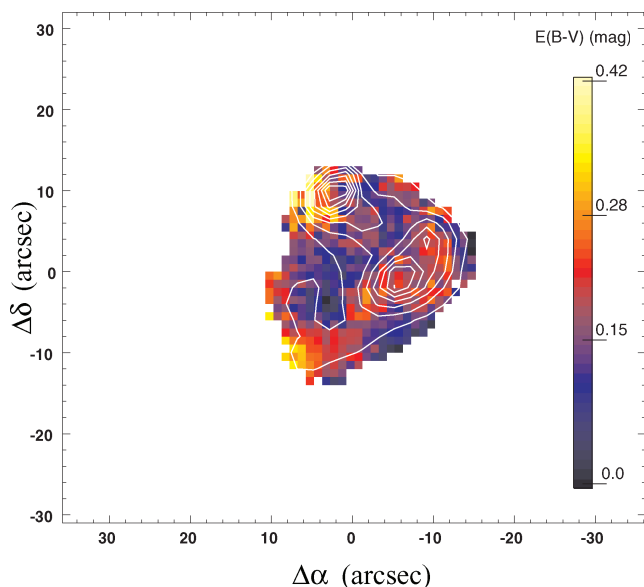


Figure 5. PPAK total colour excess map computed from the Balmer emission-line ratio $F(\text{H}\alpha)/F(\text{H}\beta)$ using Cardelli extinction law. $\text{H}\alpha$ emission is shown in white contours.

the Balmer line ratio $\text{H}\alpha/\text{H}\beta$. The departure from the measured $\text{H}\alpha/\text{H}\beta$ ratio of the theoretically expected value is produced by the extinction of light due to a screen of homogeneously distributed interstellar dust.

$$E(B - V)_t = K\alpha\beta \log \left[\frac{\text{H}\alpha/\text{H}\beta}{2.86} \right], \quad (1)$$

where $K\alpha\beta = [-0.4[k(\text{H}\alpha) - k(\text{H}\beta)]]^{-1}$; $\text{H}\alpha/\text{H}\beta$ is the ratio of the observed $\text{H}\alpha$ and $\text{H}\beta$ emission-line fluxes; and 2.86 represents the expected $\text{H}\alpha/\text{H}\beta$ value for case B recombination at $T = 10^4$ K and electron density of 100 cm^{-3} (Osterbrock 1989). $K\alpha\beta$ depends on the selected extinction curve and takes the value 2.328 in Cardelli, Clayton & Mathis (1989).

The $\text{H}\alpha$ and $\text{H}\beta$ stellar absorption corrected fluxes are used to derive the colour excess map (see Fig. 5). The foreground Galactic reddening at the position of NGC 7673 is $E(B - V)^{\text{GAL}} = 0.04$ mag (Schlegel, Finkbeiner & Davis 1998). The PPAK colour excess map shows values in the range 0.04–0.35 mag in the majority of pixels. The dust extinction distribution seems to be related with the position of the main clumps of star formation (except for clump D) showing small spatial variations. In clumps A, B, E and F the total colour excess is $E(B - V)_t \approx 0.20 \pm 0.03$ while for clumps C and D, it is 0.16 and 0.12, respectively. In clump B we find relatively higher values for the colour excess [$E(B - V)_t \approx 0.4$] in a region displaced with respect to the maximum $\text{H}\alpha$ emission to the east direction.

These values are in agreement with the colour excess determined by Pasquali & Castangia (2008) using cluster colours in different *HST*/WFPC2 bands, where the intrinsic cluster reddening $E(B - V)_i$ found is lower than 0.4 mag with the large majority of clusters in this galaxy having $0. \leq E(B - V)_i \leq 0.25$ mag. They estimate cluster ages based on WFPC2 images and classified the clusters in three samples: young sample with ages < 2.5 Myr, intermediate one with ages in the range 2.5–8 Myr and the old sample with ages > 8 Myr. Despite the large age uncertainty, they point out that the star clusters in NGC 7673 seem to get younger as their distance in the north-east direction from clump A increases.

From the Balmer decrement we determine for the integrated galaxy spectrum $E(B - V)_t = 0.17$ mag. The extinction $A_{\text{H}\alpha}$ com-

puted from this colour excess is 0.40 mag ($A_V = 0.49$) using the extinction curve from Cardelli et al. (1989).

The UV wavelength can provide us an independent attenuation estimation. We estimate the attenuation in the FUV and NUV bands using the ratio between the total dust emission in the range 1–1000 μm (TIR) and the observed stellar emission in the FUV and NUV bands. The TIR luminosity for this galaxy was derived by Calzetti et al. (2000) from *IRAS* and *ISO* data. The FUV and NUV luminosities were taken from Gil de Paz et al. (2007). By applying the calibrations of Cortese et al. (2008) we find the attenuation in the FUV and NUV to be $A_{\text{FUV}} = 1.08$ mag and $A_{\text{NUV}} = 0.86$ mag, respectively. The slope of the UV spectrum or, equivalently, the FUV–NUV colour are known to be tightly correlated with the UV extinction in starburst galaxies (see e.g. Calzetti, Kinney & Storchi-Bergmann 1994; Meurer, Heckman & Calzetti 1999). Considering that NGC 7673 has $\text{FUV} - \text{NUV} = 0.25$, our values of A_{FUV} and A_{NUV} are fully consistent with what is expected for a starburst galaxy with that UV colour.

We can use the previous values of the attenuation in the UV to estimate the attenuation in the V band. While in both cases we are referring to the extinction in the stellar continuum, stars contributing to the optical emission are usually less embedded within the dust than those dominating the UV emission. To take this fact into account, we combine the MW extinction curve of Cardelli et al. (1989) with the simple sandwich model for dust geometry described in Boselli, Gavazzi & Sanvito (2003), resulting in $A_V = 0.35$ mag.

The extinction computed from the Balmer decrement is $A_V = 0.49$ mag. This value corresponds to the extinction for the gas; it has to be corrected with the 0.44 factor found by Calzetti et al. (1994) to be compared with the extinction derived from the UV colours. After this correction, the stellar extinction results in 0.13 mag lower compared with the attenuation in the V band using UV colours. Anyway, the 0.44 factor is found for most dusty starbursts and this is not the case for NGC 7673 as it is shown from the low extinction values computed in this section.

4.2 Star formation rates

Different SFR measures based on $\text{H}\alpha$ emission can be found in the literature for this galaxy: Schmitt et al. (2006) derived a lower limit for the SFR of $1.3 \text{ M}_\odot \text{ yr}^{-1}$ for an observed $\text{H}\alpha$ flux that was corrected for Galactic extinction but not for intrinsic reddening. In Pasquali & Castangia (2008), the observed $\text{H}\alpha$ flux from McQuade, Calzetti & Kinney (1995) is de-reddened using $E(B - V) = 0.54$ mag (derived from the Balmer decrement using $\text{H}\alpha$ and $\text{H}\beta$ fluxes in McQuade et al. 1995) and $E(B - V) = 0.36$ mag (estimated for the exponentially decaying star formation history). They finally obtained an SFR between 3.3 and $5.2 \text{ M}_\odot \text{ yr}^{-1}$. Pisano et al. (2001) derived a value of $\text{SFR} = 23.5 \text{ M}_\odot \text{ yr}^{-1}$ based on Gallego et al. (1996) long-slit spectroscopic data. After reviewing how this SFR value is obtained we find the $L(\text{H}\alpha)$ published in Gallego et al. (1996) is highly overestimated due to the aperture correction applied. The same authors revisited this object in Pérez-González et al. (2003) and the SFR derived from the $\text{H}\alpha$ imaging study is $\text{SFR} = 9 \text{ M}_\odot \text{ yr}^{-1}$. Furthermore, NGC 7673 is also a well-known luminous FIR source (Sanders & Mirabel 1996). Garland et al. (2005) derived an IR–SFR of $5.5 \text{ M}_\odot \text{ yr}^{-1}$ (*IRAS* data) in agreement with the derived SFR from the 1.4 GHz radio continuum in NGC 7673 using the prescription of Bell (2003).

From the integrated galaxy spectrum we compute a total extinction-corrected luminosity $L(\text{H}\alpha) = (7.8 \pm 1.0) \times 10^{41} \text{ erg s}^{-1}$, from which a $\text{SFR} = (6.2 \pm 0.8) \text{ M}_\odot \text{ yr}^{-1}$ is derived (using the

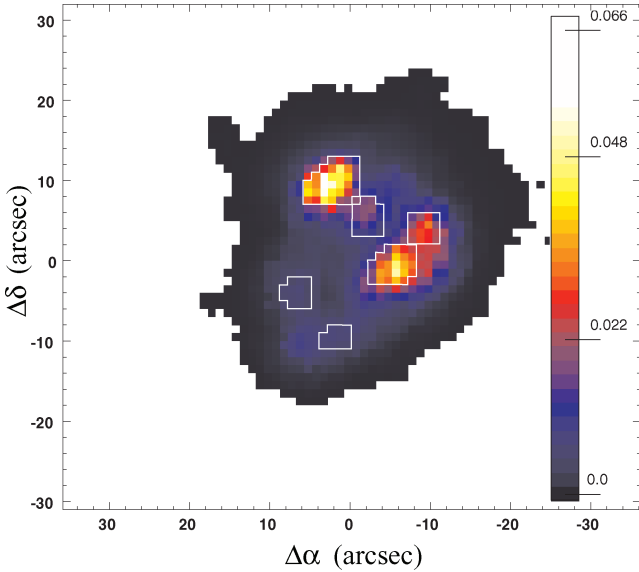


Figure 6. SFR density map in $M_{\odot} \text{ yr}^{-1} \text{ arcsec}^{-2}$ units, computed from reddening-corrected $H\alpha$ flux PPAK map. SFR are computed in regions enclosed by white colour.

relation from Kennicutt 1998a). The $H\alpha$ luminosity derived by Pérez-González et al. (2003) [$L(H\alpha) = 11.39 \times 10^{41} \text{ erg s}^{-1}$] is higher compared with our value mainly due to the absolute flux calibration (see Section 2) and the extinction correction applied. They used the ratio $F(H\alpha)/F(H\beta) = 4.21$ to correct the observed fluxes, and we find for the integrated galaxy spectrum the ratio $F(H\alpha)/F(H\beta) = 3.4$. Our $H\alpha$ -based SFR estimation is in agreement with the SFR derived from infrared and radio continuum fluxes (Garland et al. 2005, $\text{SFR} = 5.5 M_{\odot} \text{ yr}^{-1}$).

The SFR can also be estimated from the $[\text{O II}]\lambda 3727$ luminosity. We use the Kennicutt (1998a) relation $[\text{SFR}(M_{\odot} \text{ yr}^{-1})] = (1.4 \pm 0.4) \times 10^{-41} L([\text{O II}]) (\text{erg s}^{-1})$, where the observed $[\text{O II}]$ luminosity must be corrected for extinction; in this case the extinction at $H\alpha$ because of the manner in which the $[\text{O II}]$ fluxes were calibrated to obtain that relation. We compute a total $[\text{O II}]$ -based SFR of $8.5 M_{\odot} \text{ yr}^{-1}$, resulting in the range $6.1\text{--}11.0 M_{\odot} \text{ yr}^{-1}$ when we take into account the error associated with the relation $L([\text{O II}])\text{--SFR}$.

We derive an SFR surface density map based on $H\alpha$ extinction-corrected PPAK fluxes (see Fig. 6) using the relation in Kennicutt (1998a). The star formation is located mainly in clumps A, B, C and F as can be seen in Fig. 6. Clump B shows the highest $H\alpha$ luminosity with an SFR surface density of $0.52 M_{\odot} \text{ yr}^{-1} \text{ kpc}^{-2}$. Clumps D and E are regions with low $H\alpha$ luminosity and their contribution to the total SFR is not significant. Although clump E was selected in this work for comparison reasons with the results by Dufloc-Augarde & Alloin (1982), this region is not associated with any star-forming region in particular, showing a low SFR. More than 50 per cent of the total SFR in this galaxy is not located in the defined clumps. The SFRs derived from the integrated galaxy spectrum and the spectra corresponding to the different clumps marked in Fig. 6 are tabulated in Table 2.

4.3 Emission-line ratio maps

We have computed different emission-line ratio maps (i.e. $[\text{O III}]\lambda 5007/H\beta$, $[\text{N II}]\lambda 6584/H\alpha$, $[\text{S II}]\lambda 6716/H\alpha$) to study the possible presence of an AGN or signs of shocks in this galaxy (see Fig. 7).

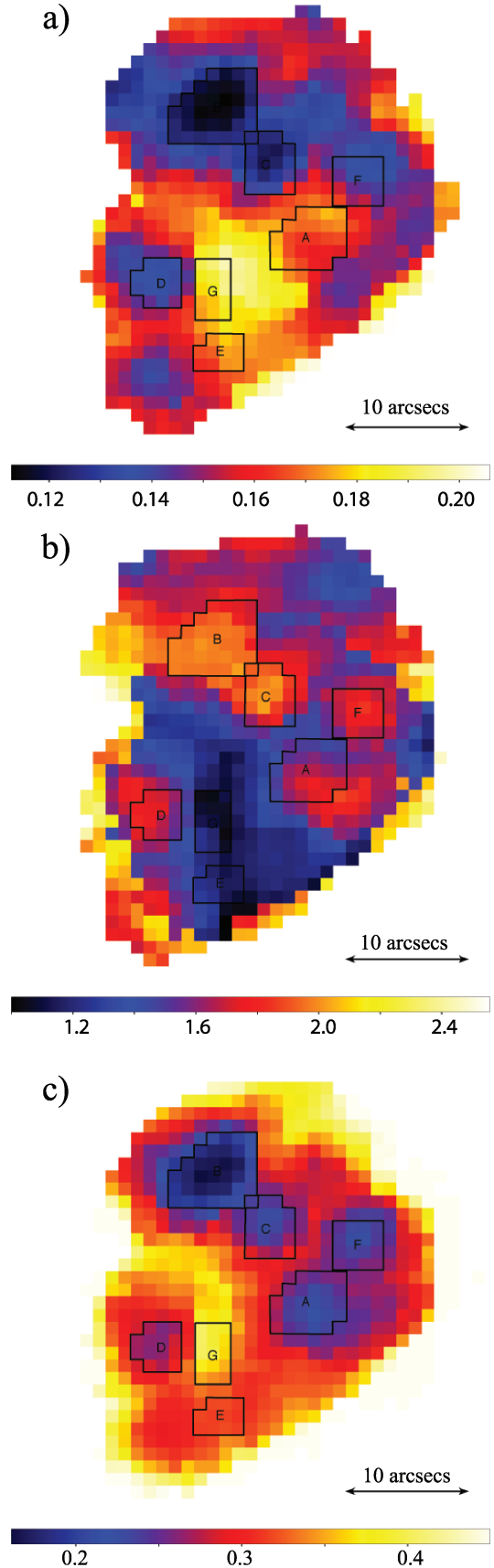


Figure 7. PPAK emission-line ratio maps: (a) $[\text{N II}]\lambda 6584/H\alpha$, (b) $[\text{O III}]\lambda 5007/H\beta$ and (c) $[\text{S II}]\lambda\lambda 6716, 6731/H\alpha$. The position of the main clumps is overlaid.

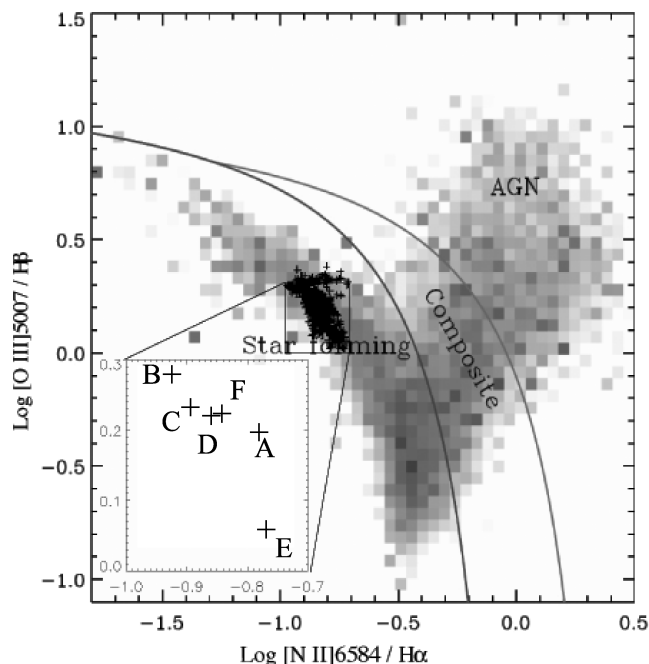


Figure 8. Diagnostic diagram $[N II]\lambda 6584/H\alpha$ versus $[O III]\lambda 5007/H\beta$ is shown for SDSS galaxies (grey pixels) from Brinchmann et al. (2004). The values for every pixel in the PPAK map are included in black crosses. The location of clumps A–F is also shown in an included figure.

The position of the different clumps except for clump E is very well traced in the $[S II]/H\alpha$ map with clumps corresponding to regions of low emission-line ratio (0.24). Clump B in this map shows the lowest value (0.18) and clump D the highest one (0.27). Region G is defined as a new region between clumps A and D. In this region the presence of the underlying stellar population is most noticeable (see Fig. 4 of absorption stellar equivalent width) and the $[S II]/H\alpha$ ratio reaches the value of 0.40. The map corresponding to the ratio $[O III]\lambda 5007/H\beta$ shows higher values, corresponding to higher ionization regions, at the position of clumps with values of 1.6, showing a slightly higher value 1.9 at the position of clump B. The different clumps show values of $[N II]\lambda 6584/H\alpha$ very similar in the range 0.12 (for clump B) and 0.17 (for clump A). Only region G shows a higher value of 0.20 for this ratio. Dufloc-Augarde & Alloin (1982) found a similar distribution of the $[N II]\lambda\lambda 6458, 6584/H\alpha$ ratio. In their analysis they computed the highest ratio value in clump A and lowest one in clump B. In Fig. 8, the diagnostic diagram $[N II]\lambda 6584/H\alpha$ versus $[O III]\lambda 5007/H\beta$ is shown for every pixel in the PPAK map. For comparison, the values for SDSS galaxies are plotted in the same figure. We find values of $[N II]\lambda 6584/H\alpha$ ratio in the range 0.1–0.2 and $[O III]\lambda 5007/H\beta$ values in the range 1–2.5. The location of clumps A–F in this diagram is shown in the same figure and situate the clumps in a sequence of metallicity [as suggested by the several sets of theoretical photoionization models described in Dopita & Evans (1986)] where clumps E³ and A would have higher metallicity values, clumps C, D and F intermediate metallicity values and clump B the lowest one. These ratio values (see Table 2) are clearly in agreement with those of H II regions of intermediate metallicity and with no signs of AGN activity (Osterbrock 1989). The $[S II]/H\alpha$ map is also computed showing

³ Actually, clump E, although defined in Dufloc-Augarde & Alloin (1982), is not associated with any $H\alpha$ emission region in particular.

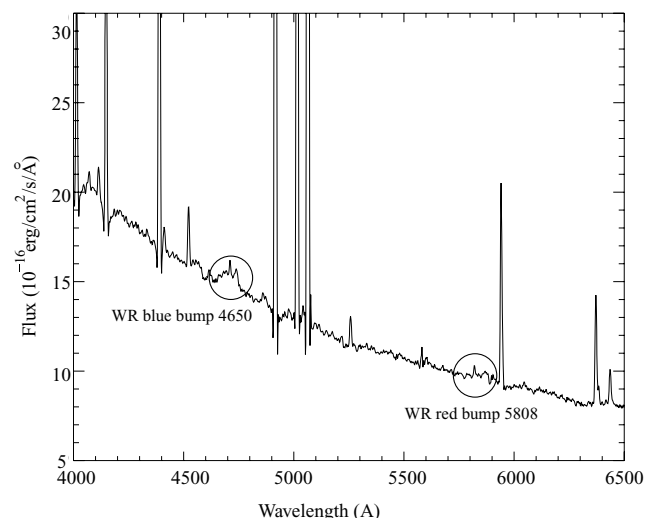


Figure 9. Sum of the spectra in clump B where the WR stellar population is detected. The blue and red WR bumps can be observed.

values <0.4 for all the pixels. The location of these values in the diagnostic diagram $[S II]/H\alpha$ versus $[N II]\lambda 6584/H\alpha$ is compatible with a starburst galaxy (see fig. 12 in Rickes, Pastoriza & Bonatto 2008) ruling out the presence of low ionization nuclear emission region (LINER) or shocks as the ionization source in this galaxy.

4.4 Wolf–Rayet stellar population

Wolf–Rayet (WR) stars are evolved, massive stars, which are losing mass rapidly by means of a very strong stellar wind (Maeder & Conti 1994). The presence of WR stars can be inferred from the detection of WR bumps around $\lambda 4650 \text{ Å}$ (blue bump) and $\lambda 5808 \text{ Å}$ (red bump), which are generally a blend of He II and several metal lines.

We detect the presence of WR stellar population in NGC 7673. The blue and red WR bumps can be observed in several fibres at the position of clump B. The sum of the spectra where WR bumps are detected is shown in Fig. 9. The WR bumps intensity maximum coincides spatially with the position of $H\alpha$ peak emission in clump B. The detection of a WR stellar population at this clump indicates this is a young (less than 4 Myr) burst of massive stars. In agreement with this detection Pasquali & Castangia (2008) found cluster ages younger than 2.5 Myr and in the range 2.5–8 Myr for the majority of star clusters located in clump B.

4.5 Metallicity

Dufloc-Augarde & Alloin (1982) determined almost a constant oxygen abundance in the clumps studied in NGC 7673 ($12 + \log(O/H) \approx 8.6$) using empirical methods described by Alloin et al. (1979) and Pagel et al. (1979). Storch-Bergmann, Calzetti & Kinney (1994) obtained a similar value of oxygen abundance ($12 + \log(O/H) = 8.48$) using the calibration diagrams from Pagel et al. (1979) to obtain $T[O III]$.

A precise measurement of the weak auroral forbidden emission line $[O III]\lambda 4363$ is needed to give an accurate determination of oxygen abundance in gaseous ionized nebulae. This emission line which is temperature sensitive correlates with the overall abundance (Osterbrock 1989), being relatively strong in very low metallicity systems but undetectable for even moderately low metallicity galaxies [$12 + \log(O/H) > 8.3$] (Denicoló, Terlevich & Terlevich 2002).

We inspected all the spectra in NGC 7673 and for some fibres the detection of the emission line $[\text{O III}]\lambda 4363$ is possible with enough S/N (5σ -level). In particular we are able to detect $[\text{O III}]\lambda 4363$ in a few spectra corresponding to clump B where the stellar absorption over the $\text{H}\gamma$ emission is not so important and the emission flux for $[\text{O III}]\lambda 4363$ can be measured reliably. We apply the T_e -method to measure gas metallicity, using the routine ABUND of the NEBULAR package of the STSDAS/IRAF for this task. We assume a two-zone model for the star-forming nebula, a medium-temperature zone where oxygen is doubly ionized and a low-temperature zone where oxygen is assumed to be singly ionized and neutral. The electron temperature in the medium-temperature zone, $T_e(\text{O III})$ is derived from the $[\text{O III}](\lambda 4959 + \lambda 5007)/\lambda 4363$ line intensity ratio (Izotov, Thuan & Lipovetsky 1994). The temperature in the low-temperature zone, $T_e(\text{O II})$, is estimated using the relation $t_e(\text{O II}) = 2[t_e(\text{O III})^{-1} + 0.8]^{-1}$, proposed by Pagel et al. (1992) based on H II region models of Stasińska (1990), where t_e are temperatures measured in units of 10^4 K. The electron density (N_e) is estimated from the $[\text{S II}]\lambda 6716/\lambda 6731$ ratio. The computed total oxygen abundance is the sum of all measured oxygen ionic abundance, considering negligible the contribution of O^{3+} to the total abundance.

The error estimation for the oxygen abundance comes mainly from the uncertainty in the $[\text{O III}]\lambda 4363$ emission flux. We estimate 10–18 per cent relative error in this emission flux. We compute new electronic temperatures taking into account this uncertainty, and derive new oxygen abundances. Relative errors in temperature range from 4 to 7 per cent and result in final metallicity errors of 0.04–0.07 dex.

In some fibres located at clump B, we use the S/N of each spectrum to find an upper limit to the $[\text{O III}]\lambda 4363$ line strength in the case this auroral line is not detected. With this estimation we can derive an upper limit to the electron temperature and hence a lower limit for the oxygen abundance.

The oxygen abundance computed in clump B is in the range $12 + \log(\text{O}/\text{H}) = 7.96\text{--}8.10$, with a value of $12 + \log(\text{O}/\text{H}) = 8.07 \pm 0.04$ ($\approx 1/4$ solar⁴) for the fibre at the position of the maximum $\text{H}\alpha$ intensity. Furthermore, the oxygen abundance derived from the sum of spectra in clump B is $12 + \log(\text{O}/\text{H}) = 8.02 \pm 0.05$. We attempted to find an estimation of the metallicity summing up the signal from different fibres around clump B. In this case the $[\text{O III}]\lambda 4363$ line strength is difficult to measure due to the position of this emission line near to the $\text{H}\gamma$ absorption stellar wing. Nevertheless, we estimate a lower limit for the oxygen abundance in the surroundings of clump B of $12 + \log(\text{O}/\text{H}) > 7.87$.

A metallicity estimation for the rest of regions in this galaxy is obtained using the R23 index [$\text{R23} = \log([\text{O II}]\lambda 3727 + [\text{O III}]\lambda\lambda 4959, 5007)/\text{H}\beta$]. We apply the R23 method described in Kewley & Dopita (2002) for the low-metallicity region, taking into account the ionization parameter. From the spectrum corresponding to each clump, we derived an initial guess for the metallicity using the $[\text{O II}]/[\text{O III}]$ and $[\text{N II}]/[\text{S II}]$ emission-line ratios (Charlot & Longhetti 2001). Taking a metallicity estimation for each clump, the first estimation of the ionization parameter is derived from the $[\text{O III}]/[\text{O II}]$ ratio. The R23 index is then used to determine the oxygen abundance and if this value is significantly different from the initial metallicity guess, the ionization parameter is again computed with the new metallicity estimation. This process is repeated until

Table 3. Metallicity estimations for each region derived from the R23 index. Col. 1: name of each region. Col. 2: $\text{R23} = \log([\text{O II}]\lambda 3727 + [\text{O III}]\lambda\lambda 4959, 5007)/\text{H}\beta$ values with typical error of 0.07 dex. Col. 3: derived oxygen metallicity using R23 method described in Kewley & Dopita (2002) for the low-metallicity region, taking into account the ionization parameter. Col. 4: measured M_B (corrected for Galactic extinction) in magnitudes with typical error of 0.1 mag.

Region	R23	$12 + \log(\text{O}/\text{H})$	M_B
NGC 7673	0.72	8.20 ± 0.15	-20.2
Clump A	0.68	8.12 ± 0.12	-17.9
Clump B	0.73	8.23 ± 0.15	-17.3
B Surroundings	0.76	8.30 ± 0.20	–
Clump C	0.73	8.21 ± 0.16	-16.9
Clump D	0.69	8.14 ± 0.12	-15.6
Clump E	0.69	8.15 ± 0.14	-15.3
Clump F	0.73	8.21 ± 0.16	-16.7
Region G	0.64	8.07 ± 0.11	–

there is no significant change in the metallicity value which usually happens after the first iteration. The R23 values and the oxygen abundance estimations for different regions in NGC 7673 are shown in Table 3. Fig. 10 shows the R23 map with values in the range 0.6–0.8. For the integrated galaxy spectrum we derive $\text{R23} = 0.72 \pm 0.07$ and $q = 2 \times 10^7 \text{ cm s}^{-1}$ which gives $12 + \log(\text{O}/\text{H}) = 8.20 \pm 0.15$, lower than previous works. Duflot-Augarde & Alloin (1982) found oxygen abundance of $12 + \log(\text{O}/\text{H}) = 8.45$ for clump A and $12 + \log(\text{O}/\text{H}) = 8.60$ for clump B using the empirical method based on the $([\text{O II}] + [\text{O III}])/\text{H}\beta$ line intensity ratio and the opposite values when the $[\text{O III}]/[\text{N II}]$ ratio is employed. They considered the two empirical methods provide abundances in good agreement taking into account the uncertainty inherent to this kind of analysis.

For comparison we computed the R23 oxygen abundance in those fibres where we detect $[\text{O III}]\lambda 4363$ (see Fig. 10 and Table 4). The R23 method overestimates the oxygen abundance in fibres 1, 2 and 5 (differences of 0.14–0.40 dex). The two methods give similar results in fibres 4 and 9 where the S/N in the $[\text{O III}]\lambda 4363$ detection is higher suggesting that the R23 method is reliable. For the remaining fibres (3, 6, 7, 8 and 10) where the $[\text{O III}]\lambda 4363$ auroral line is not detected we only estimate lower limits for the abundances derived with the T_e method.

In conclusion, for clump A which dominates the galaxy morphology we derive a low R23 metallicity estimation (0.27 solar). Clump B seems to be surrounded by a region which shows marginally higher metallicity (0.41 solar) compared with the metallicity derived in clump B (0.35 solar) from the same method R23. Clumps D and E with the same metallicity estimation (0.28 solar) seem to belong to the same spiral arm. Finally, clumps C and F situated at equidistant positions with respect to clump A have the same derived metallicities (0.33 solar).

5 DISCUSSION

5.1 Nucleus

The location of the nucleus in NGC 7673 is not well determined. Homeier & Gallagher (1999) refer to clump A as the ‘nucleus’. If this is true we would expect a specific behaviour in the kinematic, velocity width maps and diagnostic diagrams. From the analysis of the $\text{H}\alpha$ kinematic map PG10 find the position of the kinematic centre in between clumps C and A. This location corresponds to the position of a maximum found in the gas velocity width map and

⁴ We consider $[12 + \log(\text{O}/\text{H})]_{\odot} = 8.69$ (Allende Prieto, Lambert & Asplund 2001).

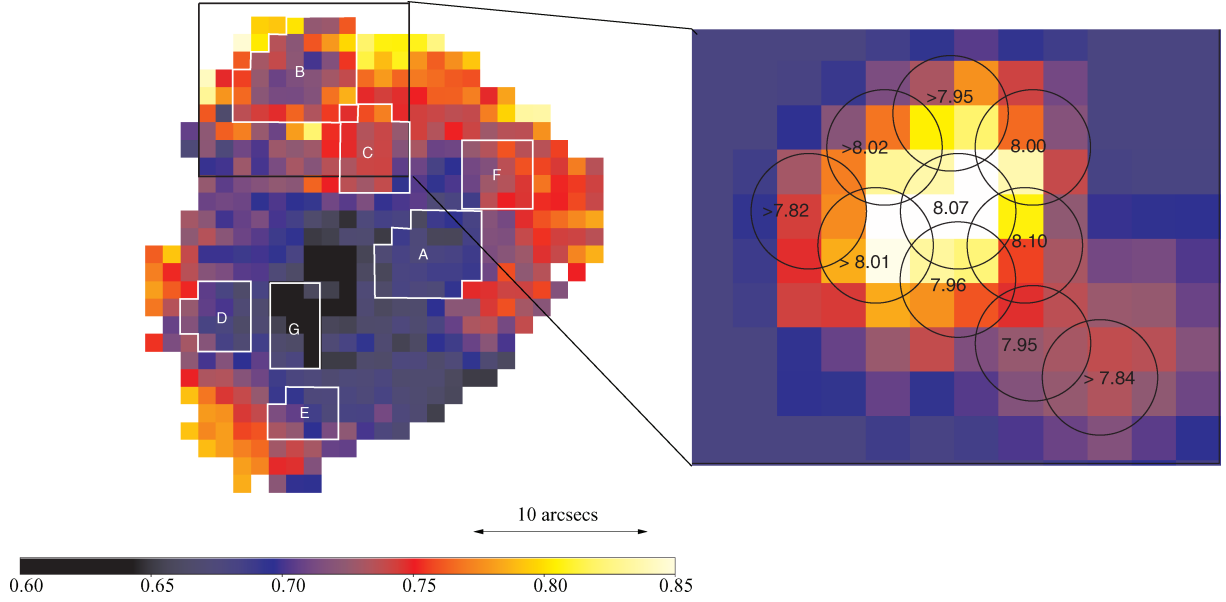


Figure 10. Left: $R23 = \log([O\text{II}]\lambda 3727 + [O\text{II}]\lambda 4959, 5007)/H\beta$ map with regions where the oxygen metallicity (using R23 index) is computed overlaid. Right: detail of the $H\alpha$ emission in clumps B and C. The position of some fibres with the computed oxygen metallicity is overlaid. Oxygen metallicity ($12 + \log(O/H)$) is derived in five fibres located at clumps B and C where the emission line $[O\text{II}]\lambda 4363$ is detected (5σ -level). In some fibres we compute a metallicity lower limit.

Table 4. Metallicity estimations for each fibre in Fig. 10 derived from the T_e -method and R23 ratio as explained in Section 4.5. Col. 1: fibre number. Col. 2: Oxygen metallicity computed from T_e -method. Col. 3: Derived oxygen metallicity using R23 method.

Fibre	$12 + \log(O/H)_{T_e}$	$12 + \log(O/H)_{R23}$
1	7.96 ± 0.05	8.14 ± 0.14
2	8.00 ± 0.05	8.14 ± 0.14
3	> 8.02	8.33 ± 0.25
4	8.07 ± 0.04	8.06 ± 0.11
5	7.95 ± 0.06	8.35 ± 0.27
6	> 7.82	8.31 ± 0.22
7	> 8.01	8.11 ± 0.13
8	> 7.95	8.28 ± 0.19
9	8.10 ± 0.05	8.07 ± 0.12
10	> 7.84	8.12 ± 0.13

roughly coincides with the photometric and geometric centres of the galaxy.

This latter finding does not, however, rule out the possibility for clump A to host the nucleus. Indeed, our computed extinction map shows at the position of clump A a concentration of extinction although with not very high values. Probably, the nucleus of this galaxy is located in this clump but the optical light does not penetrate enough to reveal the optical counterpart of the nucleus.

Radio continuum emission in this galaxy might help to locate the position of the nucleus. Condon & Yin (1990) show VLA data (A-array at 1.46 GHz) mapped at 3 and 1.5 arcsec angular resolution. These radio continuum images show an irregular, diffuse morphology characteristic of a starburst with the two brightest radio peaks matching up the brightest optical clumps A and B. But there is no radio peak emission at the position of the kinematic centre found in PG10. Furthermore, in their high-resolution radio map there is no evidence of any compact source stronger than $S=0.5$ mJy or of radio jets powered by a nuclear AGN.

When we represent clump A in several diagnostics diagrams we find no sign of any AGN activity (see Fig. 8). Mid-IR spectra can shed further light on the AGN versus starburst nature of the galaxy. In particular, the emission features due to Polycyclic Aromatic Hydrocarbons (PAHs) are known to be much weaker in AGNs than in starburst galaxies (see e.g. Weedman & Houck 2009, and references therein). In the particular case of NGC 7673, mid-IR spectra from the Infrared Spectrograph (IRS, Houck et al. 2004) onboard *Spitzer* (Werner et al. 2004) are publicly available in the *Spitzer* archive (program ID 73, PI: J. R. Houck). We used the tool CUBISM (Smith et al. 2007) to build and inspect the corresponding data cube. PAH features are visible across the whole galaxy, and are particularly bright in clump A, whose spectrum resembles the starburst templates presented in Weedman & Houck (2009). Moreover, we do not observe strong high-ionization lines of $[\text{Ne}\text{V}]$ or $[\text{O}\text{IV}]$ which, if present, would point towards an AGN as the primary ionizing source. Therefore, the mid-IR data support the starburst nature of this galaxy.

5.2 The peculiarity of clump B

Different properties measured in clump B make this region peculiar. This clump with bluer colour ($M_B = -17.3$) and medium-high SFR density ($0.5 M_\odot \text{ yr}^{-1} \text{ kpc}^{-2}$) represents a compact decoupled kinematic component studied in detail by PG10. The *HST* image of this galaxy shows B region to be clumpy with a central peak of emission surrounded by two bright shells. Its bubble morphology is probably the result of the stellar winds associated with massive stars. Indeed, we detect the presence of WR stellar population in several fibres in clump B pointing out the presence of massive stars, where young (less than 2.5 Myr old) and intermediate-age clusters (between 2.5 and 8 Myr) are found (Pasquali & Castangia 2008).

While at the centre of clump B we find extinction values similar to clumps A and F, relatively higher values for the colour excess $[E(B - V)]_t \approx 0.4$ are found in a region displaced with respect to the maximum $H\alpha$ emission to the east direction. Our measurements of

the equivalent width of the underlying stellar population absorption features (e.g. $H\beta$, $H\gamma$) show a peculiarity at the location of clump B. The strength of these features is noticeable throughout the galaxy but it is almost absent at the location of clump B (see Fig. 4). The strength of the equivalent width of these features account for the age of the underlying population. Strong lines are mainly due to a population of A class stars and correspond to systems a few hundred thousand years old. Weaker lines are typical of either younger or older populations. None the less, clump B shows signs of differentiation, at least marginally, with respect to its environment from the point of view of both, the gas and the stars.

From our metallicity study clump B is a region with low metallicity ($\approx 1/4$ solar) surrounded by a region with marginally higher metallicity (see Fig. 10). Furthermore, a detailed study using the R23 index shows some fibres at the east side of the central fibre in clump B with higher metallicity (≈ 1.2 solar). This region is located at the position where PG10 find maximum values for the velocity width.

The location of NGC 7673 in the luminosity–metallicity relation is in agreement with the trend observed for intermediate- z star-forming galaxies from Salzer, Williams & Gronwall (2009) and from intermediate- z LCBGs from Hoyos et al. (2005) (see PG10). But the properties of clump B, being less luminous and with approximately the same metallicity, positioned this region closer to the dwarf irregulars trend (Richer & McCall 1995) as already seen in PG10. But this region could also be a nearby giant H II region following the $H\beta$ luminosity–velocity width correlation by Melnick et al. (1987). Nevertheless, as explained in PG10, clump B is brighter and more massive than any of the nearby giant H II regions within their sample, suggesting that an in-falling dwarf galaxy rather than a giant H II region might be the reason for the peculiarities found in this clump.

In summary, our 3D data show clump B is a compact region kinematically decoupled with high extinction and SFR density and with luminosity and metallicity properties that suggest a dwarf galaxy or a giant H II region nature for this clump.

5.3 On the nature of NGC 7673

The star formation activity in this LCBG galaxy is located in several clumps as it is shown in the SFR surface density map. In general, the origin of the starburst activity could be explained by different mechanisms which include interactions and mergers (Schweizer 1987; Jog & Das 1992), bar instabilities (Shlosman, Begelman & Frank 1990) and kinematic from SNe and stellar winds (Heckman, Armus & Miley 1990). Although Homeier & Gallagher (1999) excluded an active interaction of NGC 7673 with its companion NGC 7677 as the starburst trigger, they cannot rule out a past interaction. Another possibility suggested by these authors is the capture of a dwarf companion in a minor merger as the main starburst triggering which would account for the presence of the different bursts and the characteristic morphology in this galaxy.

The *HST* image of this galaxy⁵ shows a clearly distorted morphology with an inner disturbed spiral structure. Clump A dominates the galaxy morphology and probably the nucleus of NGC 7673 is hidden by extinction at this position. The ring-like shape with the absence of $H\alpha$ emission at the centre of clump D (as seen in the high spatial resolution map) shows this is an evolved star-forming region decoupled from the spiral structure where region E is located.

Our kinematic study in PG10 shows an asymmetrical ionized gas velocity map, where a decoupled kinematic component is found at the position of clump B. This region is peculiar not only from the kinematic study but also from different physical properties derived in this paper. This region, with the highest $H\alpha$ emission equivalent width and star formation surface density, is composed of young (we detect the presence of WR stellar population) and intermediate-age clusters where the underlying stellar population shows the absence of strong absorption features. We find no evidence for either AGN activity (see Section 4.3) or SNe galactic winds (PG10) in this kinematically decoupled component, and from the metallicity and luminosity derived in this work, clump B is in agreement with being an extremely giant H II region or an in-falling dwarf galaxy (see PG10).

As stated in Homeier & Gallagher (1999), NGC 7673 and NGC 3310 present morphological and spectroscopic similarities in H II and H I data which would lead us to think in the same triggering scenario for both starburst galaxies. NGC 3310 has been largely classified as a system which is undergoing a minor merger with a dwarf companion (see e.g. Mulder & van Driel 1996). A similar scenario would account for the inner bursts in NGC 7673 and the different morphological features, such as arcs, in its outer parts. The spectroscopic and kinematic properties derived for clump B in this work and in PG10 would lead us to think that this decoupled kinematic component is the dwarf satellite galaxy in the minor merger hypothesis although this needs to be confirmed with further studies. While Homeier & Gallagher (1999) talk about a past minor merger to allow the outer disc to mostly recover, the similarities with NGC 3310, the position of the decoupled kinematic component in the galaxy disc and the young and intermediate age of its starburst seem to support an on-going interaction.

6 SUMMARY

Physical properties of the star-forming regions in the local LCBG NGC 7673 are studied in detail using 3D data taken with the PPAK integral field unit at the 3.5-m telescope in the Centro Astronómico Hispano Alemán. From previous ground-based images six main clumps have been identified in this galaxy being four of the clumps strong $H\alpha$ sources (A, B, C and F). We derive integrated and spatially resolved properties such as extinction, SFR and metallicity for this galaxy and our results are the following.

(1) Our data show an extinction map with maximum values located at the position of the main clumps of star formation showing small spatial variations. The colour excess values for the different clumps are in the range $E(B - V)_i = 0.12\text{--}0.21$ mag (0.17 mag for the integrated galaxy spectrum), in agreement with the results from Pasquali & Castangia (2008).

(2) We derive an $H\alpha$ -based SFR for this galaxy of $6.2 \pm 0.8 M_{\odot} \text{ yr}^{-1}$ in agreement with the SFR derived from infrared and radio continuum fluxes (Garland et al. 2005). The star formation is located mainly in clumps A, B, C and F. Different properties measured in clump B make it peculiar. We find for this burst the highest $H\alpha$ luminosity with an SFR surface density of $0.5 M_{\odot} \text{ yr}^{-1} \text{ kpc}^{-2}$. This region shows the absence of strong absorption features and the presence of WR stellar population indicating this is a young burst of massive stars. The analysis of the emission-line ratios discards the presence of any AGN activity or shocks as the ionization source in this clump or any other in this galaxy.

(3) Furthermore, we estimate a gas metallicity of $12 \pm \log(\text{O}/\text{H}) = 8.20 \pm 0.15$ (0.32 solar) for the integrated galaxy

⁵ <http://www.spacetelescope.org/images/html/heic0205a.html>

using the R23 index. The values derived for the different clumps with this method show a small metallicity variations in this galaxy, with values in the range 8.12 (for clump A) to 8.23 (for clump B) for $12 + \log(\text{O}/\text{H})$.

The detection (5σ -level) of the auroral forbidden emission line $[\text{O III}]\lambda 4363$ in some fibres located in clump B allows us to determine metallicities using the T_e -method and compare these values with the computed R23 oxygen abundance for the same fibres. Although in some cases the R23 index overestimates the oxygen abundance (differences of 0.14–0.40 dex), in those fibres with higher S/N in the $[\text{O III}]\lambda 4363$ detection both methods give similar results suggesting the reliability of the R23 method.

(4) Between the possible mechanisms to explain the starburst activity in this galaxy, our 3D spectroscopic data support the scenario in which a minor merger is taking place with the possibility for clump B, a compact decoupled kinematic component, to be a dwarf satellite galaxy.

ACKNOWLEDGMENTS

We are grateful to the anonymous referee for his valuable comments which have led to an improvement in this paper. We acknowledge support from the Spanish Programa Nacional de Astronomía y Astrofísica under grants AYA2006-02358 and AYA2006-15698-C02-02. This work is partially funded by the Spanish MICINN under the Consolider-Ingenio 2010 Program grant CSD2006-00070: First Science with the GTC. ACM acknowledges support from the Juan de la Cierva Program financed by the Spanish MICINN. JPG acknowledges support from a University of Florida Alumni Fellowship and RG from NASA Grant LTSA NA65-11635. SFS thanks the subprograms of *Viabilidad, Diseño, Acceso y Mejora de ICTS* ICTS-2009-10 and the *PAI Proyecto de Excelencia* P08-FWM-04319 and the funds of the PAI research group FQM360. SFS thanks the Spanish Plan Nacional de Astronomía a program AYA2005-09413-C02-02.

REFERENCES

Adelman-McCarthy J. K. et al., 2006, *ApJS*, 162, 38
 Allende Prieto C., Lambert D. L., Asplund M., 2001, *ApJ*, 556, L63
 Alloin D., Collin-Souffrin S., Joly M., Vigroux L., 1979, *A&A*, 78, 200
 Bell E. F., 2003, *ApJ*, 586, 794
 Boselli A., Gavazzi G., Sanvito G., 2003, *A&A*, 402, 37
 Brinchmann J., Charlot S., White S. D. M., Tremonti C., Kauffmann G., Heckman T., Brinkmann J., 2004, *MNRAS*, 351, 1151
 Calzetti D., Kinney A. L., Storch-Bergmann T., 1994, *ApJ*, 429, 582
 Calzetti D., Armus L., Bohlin R. C., Kinney A. L., Koornneef J., Storch-Bergmann T., 2000, *ApJ*, 533, 682
 Cardelli J. A., Clayton G. C., Mathis J. S., 1989, *ApJ*, 345, 245
 Castellanos M., 2000, PhD thesis, Universidad Autónoma de Madrid
 Charlot S., Longhetti M., 2001, *MNRAS*, 323, 887
 Condon J. J., Yin Q. F., 1990, *ApJ*, 357, 97
 Cortese L., Boselli A., Franzetti P., Decarli R., Gavazzi G., Boissier S., Buat V., 2008, *MNRAS*, 386, 1157
 Denicoló G., Terlevich R., Terlevich E., 2002, *MNRAS*, 330, 69
 Dopita M. A., Evans I. N., 1986, *ApJ*, 307, 431
 Dufout-Augarde R., Alloin D., 1982, *A&A*, 112, 257
 Förster Schreiber N. M. et al., 2006, *ApJ*, 645, 1062
 Gallego J., Zamorano J., Rego M., Alonso O., Vitoros A. G., 1996, *A&AS*, 120, 323
 Garland C. A., Williams J. P., Pisano D. J., Guzmán R., Castander F. J., Brinkmann J., 2005, *ApJ*, 624, 714
 Garland C. A., Pisano D. J., Williams J. P., Guzmán R., Castander F. J., Sage L. J., 2007, *ApJ*, 671, 310

Gil de Paz A. et al., 2007, *ApJS*, 173, 185
 Guzmán R., Gallego J., Koo D. C., Phillips A. C., Lowenthal J. D., Faber S. M., Illingworth G. D., Vogt N. P., 1997, *ApJ*, 489, 559
 Guzmán R., Jangren A., Koo D. C., Bershadsky M. A., Simard L., 1998, *ApJ*, 495, L13
 Hammer F., Gruel N., Thuan T. X., Flores H., Infante L., 2001, *ApJ*, 550, 570
 Heckman T. M., Armus L., Miley G. K., 1990, *ApJS*, 74, 833
 Homeier N. L., Gallagher J. S., 1999, *ApJ*, 522, 199
 Homeier N., Gallagher J. S., III, Pasquali A., 2002, *A&A*, 391, 857
 Houck J. R. et al., 2004, *ApJS*, 154, 18
 Hoyos C., Koo D. C., Phillips A. C., Willmer C. N. A., Guhathakurta P., 2005, *ApJ*, 635, L21
 Huchra J. P., 1977, *ApJS*, 35, 171
 Huchra J. P., Vogeley M. S., Geller M. J., 1999, *ApJS*, 121, 287
 Izotov Y. I., Thuan T. X., Lipovetsky V. A., 1994, *ApJ*, 435, 647
 Jog C. J., Das M., 1992, *ApJ*, 400, 476
 Kelz A. et al., 2006, *PASP*, 118, 129
 Kennicutt R. C., Jr, 1998a, *ARA&A*, 36, 189
 Kennicutt R. C., Jr, 1998b, *ApJ*, 498, 541
 Kewley L. J., Dopita M. A., 2002, *ApJS*, 142, 35
 Kobulnicky H. A., Zaritsky D., 1999, *ApJ*, 511, 118
 Koo D. C., Bershadsky M. A., Wirth G. D., Stanford S. A., Majewski S. R., 1994, *ApJ*, 427, L9
 Kurucz R. L., 1992, in Barbuy B., Renzini A., eds, *Proc. IAU Symp. 149, The Stellar Populations of Galaxies*. Kluwer, Dordrecht, p. 225
 Lowenthal J. D. et al., 1997, *ApJ*, 481, 673
 Maeder A., Conti P. S., 1994, *ARA&A*, 32, 227
 Markarian B. E., Lipovetsky V. A., Stepanian J. A., Erastova L. K., Shapovalova A. I., 1989, *Soobshcheniya Spetsial'noj Astrofizicheskoy Observatorii*, 62, 5
 McQuade K., Calzetti D., Kinney A. L., 1995, *ApJS*, 97, 331
 Melbourne J., Phillips A. C., Harker J., Novak G., Koo D. C., Faber S. M., 2007, *ApJ*, 660, 81
 Melnick J., Moles M., Terlevich R., Garcia-Pela yo J., 1987, *MNRAS*, 226, 849
 Meurer G. R., Heckman T. M., Calzetti D., 1999, *ApJ*, 521, 64
 Mulder P. S., van Driel W., 1996, *A&A*, 309, 403
 Noeske K. G., Koo D. C., Phillips A. C., Willmer C. N. A., Melbourne J., Gil de Paz A., Papaderos P., 2006, *ApJ*, 640, L143
 Osterbrock D. E., 1989, *Astrophysics of Gaseous Nebulae and Active Galactic Nuclei*. Research supported by the University of California, John Simon Guggenheim Memorial Foundation, University of Minnesota. University Science Books, Mill Valley, CA, p. 422
 Pagel B. E. J., Edmunds M. G., Blackwell D. E., Chun M. S., Smith G., 1979, *MNRAS*, 189, 95
 Pagel B. E. J., Simonson E. A., Terlevich R. J., Edmunds M. G., 1992, *MNRAS*, 255, 325
 Pasquali A., Castangia P., 2008, *MNRAS*, 385, 468
 Pérez-Gallego J. et al., 2010, *MNRAS*, 402, 1397 (PG10)
 Pérez-González P. G., Zamorano J., Gallego J., Gil de Paz A., 2000, *A&AS*, 141, 409
 Pérez-González P. G., Zamorano J., Gallego J., Aragón-Salamanca A., Gil de Paz A., 2003, *ApJ*, 591, 827
 Phillips A. C., Guzmán R., Gallego J., Koo D. C., Lowenthal J. D., Vogt N. P., Faber S. M., Illingworth G. D., 1997, *ApJ*, 489, 543
 Pisano D. J., Kobulnicky H. A., Guzmán R., Gallego J., Bershadsky M. A., 2001, *AJ*, 122, 1194
 Puech M., Hammer F., Flores H., Östlin G., Marquart T., 2006, *A&A*, 455, 119
 Richer M. G., McCall M. L., 1995, *ApJ*, 445, 642
 Rickes M. G., Pastoriza M. G., Bonatto C., 2008, *MNRAS*, 384, 1427
 Salzer J. J., Williams A. L., Gronwall C., 2009, *ApJ*, 695, L67
 Sánchez S. F., 2004, *Astron. Nachr.*, 325, 167
 Sánchez S. F., 2006, *Astron. Nachr.*, 327, 850
 Sanders D. B., Mirabel I. F., 1996, *ARA&A*, 34, 749
 Schlegel D. J., Finkbeiner D. P., Davis M., 1998, *ApJ*, 500, 525

- Schmitt H. R., Calzetti D., Armus L., Giavalisco M., Heckman T. M., Kennicutt R. C., Jr, Leitherer C., Meurer G. R., 2006, *ApJ*, 643, 173
- Schweizer F., 1987, in Faber S. M., ed., *Nearly Normal Galaxies: From the Planck Time to the Present*. New York, Springer-Verlag, p. 18
- Shlosman I., Begelman M. C., Frank J., 1990, *Nat*, 345, 679
- Smith J. D. T. et al., 2007, *PASP*, 119, 1133
- Stasińska G., 1990, *A&AS*, 83, 501
- Steidel C. C., Giavalisco M., Pettini M., Dickinson M., Adelberger K. L., 1996, *ApJ*, 462, L17
- Steidel C. C., Adelberger K. L., Shapley A. E., Pettini M., Dickinson M., Giavalisco M., 2003, *ApJ*, 592, 728
- Storchi-Bergmann T., Calzetti D., Kinney A. L., 1994, *ApJ*, 429, 572
- Weedman D. W., 1983, *ApJ*, 266, 479
- Weedman D. W., Houck J. R., 2009, *ApJ*, 693, 370
- Werk J. K., Jangren A., Salzer J. J., 2004, *ApJ*, 617, 1004
- Werner M. W., Roellig T. L., Low F. J., Rieke G. H., Rieke M., Hoffmann W. F., Young E., Houck J. R., 2004, *ApJS*, 154, 1
- Zamorano J., Rego M., Gallego J., Vitores A. G., Gonzalez-Riestra R., Rodriguez-Caderot G., 1994, *ApJS*, 95, 387

This paper has been typeset from a $\text{\TeX}/\text{\LaTeX}$ file prepared by the author.

Copyright of Monthly Notices of the Royal Astronomical Society is the property of Wiley-Blackwell and its content may not be copied or emailed to multiple sites or posted to a listserv without the copyright holder's express written permission. However, users may print, download, or email articles for individual use.